IOP PUBLISHING INVERSE PROBLEMS

Inverse Problems **24** (2008) 035008 (21pp) doi:10.1088/0266-5611/24/3/035008

Enhancement of microwave tomography through the use of electrically conducting enclosures

Colin Gilmore and Joe LoVetri

Department of Electrical and Computer Engineering, University of Manitoba, Winnipeg, Manitoba R3T 5V6, Canada

E-mail: cgilmore@ee.umanitoba.ca and lovetri@ee.umanitoba.ca

Received 24 October 2007, in final form 2 March 2008
Published 8 April 2008
Online at stacks.iop.org/IP/24/035008

Abstract

We consider microwave tomography (MWT) where the imaging region is surrounded by an electrically conducting surface. This surface acts as both a shield from outside interference, holding tank for any possible matching media, and, in certain cases, serves to enhance the performance of electromagnetic (EM) inversion algorithms. For the 2D transverse magnetic (TM) case and where the surface consists of a perfect electrical conductor (PEC) in the shape of a circular cylinder, we formulate an appropriate Greens function which is amenable to implementation in the existing EM inversion codes. We utilize this Greens function in the multiplicative-regularized contrast source inversion (MR-CSI) method. Several different synthetic examples are used to test the performance of the inversion when the PEC surface is present and the results show that in many cases, the tomographic image is significantly improved. The reasons for the improved inversion results are an area of active research, but are likely to be due to the increased interrogation energy deposited into the imaging region. Results are also shown which demonstrate the problems which may arise if the unbounded domain Greens function is used in an MWT system that utilizes a matching medium of finite extent—a problem which is overcome by the inclusion of a PEC surface on the exterior of the MWT system.

(Some figures in this article are in colour only in the electronic version)

1. Introduction

Electromagnetic and acoustic tomography requires the inversion of a wave equation. Various inversion techniques for wave equations arising from electromagnetic and acoustic scattering imaging systems have been developed since the early 1980s. A substantial amount of research during the last decade or so has focused on the full nonlinear inversion problem. These techniques have matured to the point where researchers are taking them as serious contenders

for biomedical imaging and identification, and experimental systems have already been created that show good potential for electromagnetic imaging of limbs [8, 9] and breast tumours [15, 19]. The main advantage of full inversion, as opposed to a linearized imaging technique, is that a quantitative inversion of such material parameters as conductivity and permittivity goes a lot further toward solving the clinical identification problem, e.g. tumour or no tumour, and makes the technique much more useful for biomedical applications.

A large class of inversion techniques for wave-type equations are formulated as nonlinear optimization problems which are then solved using some iterative technique (see, e.g. [6, 20, 21]). Most of these techniques require the use of a Greens function for the particular tomographic setup and, typically, researchers have implemented these methods with the Greens function associated with a scatterer located in an unbounded homogeneous region. However, this assumption rarely matches the physical situation for proposed imaging systems. For example, several recently proposed and implemented biomedical imaging systems [15, 16, 18, 19] utilize a matching fluid contained in a tank made of material such as plexi-glass. The assumption of a homogenous background Greens function in the inversion method ignores the field distortions caused by the finite-extent matching medium, and may lead to inversion artefacts, as will be shown herein. To our knowledge only one other group has implemented MWT in an enclosed system [12].

In this paper, we consider surrounding the imaging area with an electrically conducting boundary surface that acts both as the container for the matching medium as well as a shield against external sources of radiation. The use of the conductor allows for more accurate modelling of the reflections at the tank boundary, and thus the ability to incorporate them into the imaging algorithm. While previous work has provided ways to eliminate these undesired fields [13], and take the fields into account, [14], in this paper we consider utilizing (not just removing or accounting for) the boundary reflections in the inversion algorithm. To this end, we show inversion results for identical scatters for both homogenous (infinite) and enclosed problems which show significant improvements for the enclosed case. We have found no published comparisons of the enclosed versus homogenous systems.

While the idea of using a conducting boundary to surround the imaging region in an inverse problem is not particular to any given inversion algorithm, in this paper we utilize the contrast source inversion (CSI) algorithm [6–10], due to its success in solving the inverse problem for homogenous backgrounds. The CSI method has been shown to be suitable for a wide range of MWT problems [9–11].

In this paper, results are shown for the case where the external conductive surface may be accurately modelled by a perfect electric conductor (PEC) in the shape of a circular cylinder, and the EM radiation may be accurately modelled as a 2D transverse magnetic (TM) problem. We formulate a form of the 2D circular-cylinder Greens function that is easily utilized in the existing electromagnetic code structure. While the formulation presented herein is for the 2D scalar wave equation, the idea is extendable into 3D and vector problems.

2. Imaging system and theoretical model

We consider a tomographic imaging system which is surrounded with an electrically conductive surface. A schematic of the imaging system is shown in figure 1. The conductive surface serves as both the container for any possible matching fluid and a shield from outside interference. The inclusion of the conductive surface differs from existing tomographic imaging systems, which typically have a plexi-glass or similar surface [15, 16, 18, 19]. The inclusion of the conducting enclosure considerably changes the distribution of the EM energy as compared to that of an open system. Key to the imaging system is that this distorted field is taken into

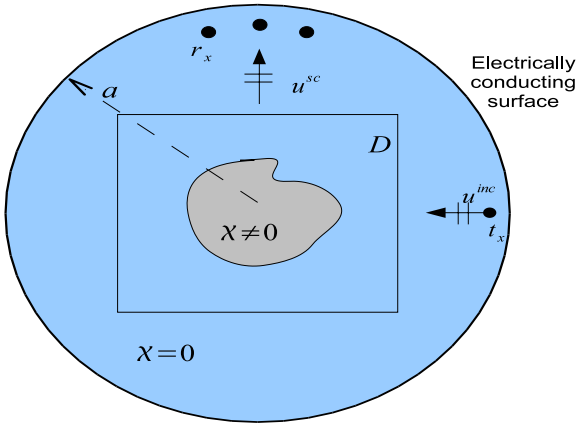

Figure 1. The enclosed imaging system. The unknown scatterer is embedded in a matching fluid which is surrounded by an electrically conductive surface. Here, the surface is shown as a circular cylinder of radius a.

account in the imaging algorithm, via the appropriate Greens function. While the shape of the surface considered herein is a cylinder, in general any shape for which a closed form of the Greens function is known may be used.

A 2D transverse magnetic (TM) (scalar) model is used throughout this paper, and the scalar field quantity (in this case, E_z) is represented with the symbol u. The conducting container is modelled as a PEC. The governing differential equation is the 2D scalar wave equation. We utilize a frequency domain model with an assumed $e^{j\omega t}$ time dependency. A series of transmitters, with positions labelled $k = 1, \ldots, K$, illuminates an unknown scatterer with an incident field denoted u_k^{inc}. The scatterer is located entirely within the region D and is embedded in a homogenous background medium with a (possibly complex for lossy media) background permittivity of ϵ_b, and a non-magnetic medium with a permeability of free space ($\mu_b = \mu_0$).

The scattered field is measured outside the region, and given by the data equation

$$u_k^{\text{sc}}(\mathbf{r}) = k_b^2 \int_D g(\mathbf{r}, \mathbf{r}')\chi(\mathbf{r}')u_k(\mathbf{r}')\,\mathrm{d}\mathbf{r}' \qquad \mathbf{r} \notin D, \tag{1}$$

where $\mathbf{r}$ is the location of the receiver, g is the background Greens function, u_k is the total field for the transmitter k, and u^{sc} is the scattered field. The background wave number is given by

$$k_b = \omega\sqrt{\epsilon_b \mu_b}, \tag{2}$$

where ω is the radial frequency. The contrast, χ is

$$\chi(\mathbf{r}) = \frac{\epsilon(\mathbf{r}) - \epsilon_b}{\epsilon_b} = \frac{k_b^2}{k^2(\mathbf{r})} - 1, \tag{3}$$

where $k^2(\mathbf{r})$ and $\epsilon(\mathbf{r})$ are the wave-number and complex permittivity inside the scattering region, respectively. The frequency dependence of permittivities, for either the scatterer or background, is assumed to arise only from the dc conductivity of the medium, and therefore we may express the real and imaginary parts of the permittivity as

$$\epsilon = \epsilon' + j\epsilon'' = \epsilon' - j\frac{\sigma}{\omega}. \tag{4}$$

For the case where the background is lossless, i.e. $\epsilon_b'' = 0$, we may express the contrast as

$$\chi(\mathbf{r}) = \chi' + j\chi'' = \frac{\epsilon'(\mathbf{r}) - \epsilon_b}{\epsilon_b} + j\frac{\epsilon''(\mathbf{r})}{\epsilon_b}. \tag{5}$$

Thus, for lossless backgrounds, the imaginary part of the contrast is non-positive.

The fields *inside* the region D are modelled by the domain equation

$$u_k(\mathbf{r}) = u_k^{\text{inc}}(\mathbf{r}) + k_b^2 \int_D g(\mathbf{r}, \mathbf{r}')\chi(\mathbf{r}')u_k(\mathbf{r}')\,\mathrm{d}\mathbf{r}' \qquad \mathbf{r} \in D, \tag{6}$$

where now $\mathbf{r}$ is located inside the scattering region D. The data (1) and domain (6) equations form a nonlinear ill-posed inverse problem for the unknown contrast, χ and the fields inside the imaging domain D.

The fundamental difference in moving from an open system to a system with a conductive enclosure is that the Greens function in the data (1) and domain (6) equations changes from a relatively simple Hankel function to a more complicated analytic expression for the Greens function of the enclosed problem. The closed form for the modified Greens function applicable to the circular cylinder is given in section 4. Many of the advantages associated with the enclosed imaging system derive from this change in the Greens function for the inverse problem.

3. The multiplicative-regularized contrast source inversion method

While the enclosed imaging system is not particular to any given inversion method, and the inverse problem may be solved in a multitude of ways, we utilize the MR-CSI method [6, 7] as it has shown extensive success as an inversion method applied to both noisy computational and experimentally collected data [8–10]. The many advantages of this inversion technique include that it does not require any *a priori* information (but it may easily be taken into account if desired), no forward solver is required in the optimization procedure, it does not require the manual selection of a regularization parameter, and it has a computational complexity of only approximately twice that of a forward solver. In addition, the MR-CSI is suitable for wide-band simultaneous multi-frequency inversion. Note that the formulation of the MR-CSI method does not depend on the particular Greens function used, and the use of a conducting enclosure does not substantially affect the method. The data equation is first re-written as

$$f_k(\mathbf{r}) = k_b^2 \int_D g(\mathbf{r}, \mathbf{r}')\chi(\mathbf{r}')u_k(\mathbf{r}')\,\mathrm{d}\mathbf{r}' \qquad \mathbf{r} \notin D, \tag{7}$$

where f_k is the measured data. It is assumed that (7) does not hold exactly, as the data are unavoidably corrupted with noise. In symbolic notation, we now write the data equation as

$$f_k(\mathbf{r}) = k_b^2 G^S \chi u_k, \tag{8}$$

where the operator G^S is defined as

$$G^S[\circ] := k_b^2 \int_D g(\mathbf{r}, \mathbf{r}')[\circ]\,\mathrm{d}\mathbf{r}' \qquad \mathbf{r} \in S, \tag{9}$$

and S is a measurement surface (or set of discrete measurement points). Similarly, the domain equation is written as

$$u_k = u_k^{\text{inc}} + G^D \chi u_k, \tag{10}$$

where the operator G^D is defined as

$$G^D[\circ] := k_b^2 \int_D g(\mathbf{r}, \mathbf{r}')[\circ]\,\mathrm{d}\mathbf{r}' \qquad \mathbf{r} \in D. \tag{11}$$

Next, define the *contrast sources*, w_k as

$$w_k(\mathbf{r}) \equiv \chi(\mathbf{r})u_k(\mathbf{r}) \qquad \mathbf{r} \in D. \tag{12}$$

By multiplying both sides of the domain equation, (10) with the contrast, χ, and utilizing the definition of the contrast sources we may write

$$\chi u_k^{\text{inc}} = w_k - \chi G^D w_k. \tag{13}$$

The CSI method formulates the inverse problem as an optimization function in two variables: the contrast, χ and the contrast sources, w. The objective function is minimized via an iterative optimization scheme. The core of the CSI method is the objective function

$$F_n = F(w_{k,n}, \chi_n) = F^S(w_{k,n}) + F^D(w_{k,n}, \chi_n), \tag{14}$$

where each term on the right-hand side is created by summing over the transmitter locations

$$F^S(w_{k,n}) = \frac{\sum_k \|\rho_{k,n}\|_S^2}{\sum_k \|f_k\|_S^2} \qquad \text{and} \qquad F^D(w_{k,n}, \chi_n) = \frac{\sum_k \|r_{k,n}\|_D^2}{\sum_k \left\|\chi_n u_k^{\text{inc}}\right\|_D^2}. \tag{15}$$

Here ρ is the data error, defined as

$$\rho_{k,n} = f_k - G^S w_{k,n} \qquad \mathbf{r} \in S, \tag{16}$$

and r, known as the domain (or object) error, is defined as

$$r_{k,n} = \chi_n u_{k,n} - w_{k,n} = \chi_n G^D w_{k,n} + \chi_n u_k^{\text{inc}} - w_{k,n} \qquad \mathbf{r} \in D. \tag{17}$$

The index $n = 1, \ldots, N$ represents the iteration number. The normalization terms in both F^S and F^D (15) are utilized to balance between the two terms in the overall objective function.

An important aspect of the CSI method is the inclusion of the domain equation inside the objective function thus obviating the need for a separate forward solver. The minimization over both unknowns χ and w is performed sequentially by taking alternating steps of the conjugate gradient minimization algorithm on each unknown. Closed-form expressions used in this minimization algorithm are available, which significantly increases the computational efficiency. The details of the minimization can be found in [6–10].

3.1. Multiplicative regularization with total variation

The CSI method may be further enhanced via the use of the multiplicative regularization (MR) which is based on minimizing the total variation of the contrast [7, 8]. It has been shown that this regularization significantly improves the performance of the algorithm in noisy environments [7] and eliminates the need for a user-selected regularization parameter, as in Tikhonov regularization (see, e.g. [9, 20]). The MR-CSI objective function becomes

$$C(w_{k,n}, \chi_n) = F_{TV}(\chi_n) F_n(w_{k,n}, \chi_n), \tag{18}$$

where

$$F_{TV}(\chi_n) = \frac{1}{A} \int_D \frac{|\nabla \chi_n(\mathbf{r})|^2 + \delta_{n-1}^2}{|\nabla \chi_{n-1}(\mathbf{r})|^2 + \delta_{n-1}^2} \, \mathrm{d}\mathbf{r}, \tag{19}$$

where A is the area of the imaging region D, $\delta_{n-1}^2 = F_{n-1}^2 \Delta^{-2}$, and Δ is the length of a side of single cell in the discretized domain (i.e. Δ^{-2} represents the reciprocal of the area of a single cell area of the domain . For example, on a rectangular grid, $\Delta^{-2} = 1/(\Delta x \Delta y)$.

In all cases considered in this paper, we utilize the multiplicative-regularized version of the CSI algorithm.

4. Derivation of the scalar Greens function for cylindrical PEC bounded imaging

In order to implement both a forward solver to generate synthetic data, and the actual MR-CSI inversion algorithm, we require an appropriate closed form of the Greens function for the enclosed homogenous region. To get this Greens function, we seek the solution to the scalar wave equation when the boundary condition is that of a circular PEC cylinder. Let the surface of the PEC cylinder be denoted by S, and the region enclosed by the cylinder as V. The governing differential equation (the wave equation) is given by

$$\nabla^2 u(\mathbf{r}) + k^2(\mathbf{r})u(\mathbf{r}) = -F(\mathbf{r}) \qquad \mathbf{r} \in V, \tag{20}$$

where u is the scalar field quantity of interest, k is the wave number (which may depend on position), F is a source term, and $\mathbf{r}$ represents position. The field quantity must also satisfy the boundary condition

$$u(\mathbf{r}; \omega) = 0 \qquad \mathbf{r} \in S \tag{21}$$

on the surrounding PEC surface.

The Greens function for a homogenous medium satisfies the equation

$$\nabla^2 g(\mathbf{r}, \mathbf{r}') + k^2 g(\mathbf{r}, \mathbf{r}') = -\delta(\mathbf{r} - \mathbf{r}') \qquad \mathbf{r} \in V. \tag{22}$$

Different Greens functions can be chosen based on the selection of the boundary conditions associated with (22). The boundary conditions may be selected to best suit a particular problem. By considering Greens second identity

$$\int_V (\phi \nabla^2 \psi - \psi \nabla^2 \phi)\, \mathrm{d}V = \oint_S \left(\phi \frac{\partial \psi}{\partial n} - \psi \frac{\partial \phi}{\partial n} \right) \mathrm{d}S, \tag{23}$$

and noting that

$$\nabla^2 u(\mathbf{r}) = -F(\mathbf{r}) - k^2 u(\mathbf{r}) \qquad \nabla^2 g(\mathbf{r}, \mathbf{r}') = -\delta(\mathbf{r} - \mathbf{r}') - k^2 g(\mathbf{r}, \mathbf{r}') \tag{24}$$

we may write

$$u(\mathbf{r}) = \int_V g(\mathbf{r}, \mathbf{r}') F(\mathbf{r}')\, \mathrm{d}\mathbf{r}' + \oint_S \left(u \frac{\partial g}{\partial n} - g \frac{\partial u}{\partial n} \right) \mathrm{d}S. \tag{25}$$

If this were a free-space problem, we could eliminate the surface integral by selecting $g = 0$ on S and requiring that g satisfies the Sommerfeld radiation condition. However, with the PEC surface, we cannot utilize these conditions. Instead, we utilize the modified Greens function method [1]. We introduce a function, $p(\mathbf{r}, \mathbf{r}')$ which satisfies the homogenous scalar Helmholtz equation

$$\nabla^2 p(\mathbf{r}, \mathbf{r}') + k^2 p(\mathbf{r}, \mathbf{r}') = 0 \qquad \mathbf{r} \in V, \tag{26}$$

and define the modified Greens function as

$$g(\mathbf{r}, \mathbf{r}') = g_{fs}(\mathbf{r}, \mathbf{r}') + p(\mathbf{r}, \mathbf{r}'), \tag{27}$$

where $g_{fs}(\mathbf{r}, \mathbf{r}')$ is the free-space Greens function (i.e. the usual Greens function in the absence of the PEC surface). It may be noted that the addition of the function p makes no contribution to the right-hand side of (22). If we now assume that g satisfies the PEC boundary condition, then we have

$$p(\mathbf{r}, \mathbf{r}') = -g_{fs}(\mathbf{r}, \mathbf{r}') \qquad \mathbf{r} \in S, \tag{28}$$

and thus the differential equation for the function p becomes

$$\begin{aligned} &\nabla^2 p(\mathbf{r}, \mathbf{r}') + k^2 p(\mathbf{r}, \mathbf{r}') = 0 \qquad \mathbf{r} \in V \\ &p(\mathbf{r}, \mathbf{r}') = -g_{fs}(\mathbf{r}, \mathbf{r}') \qquad \mathbf{r} \in S. \end{aligned} \tag{29}$$

With this construction, and the assumption that the derivative of the Greens function is finite on the surface S, the surface integral in (25) is eliminated and we get

$$u(\mathbf{r}) = \int_V g(\mathbf{r}, \mathbf{r}') F(\mathbf{r}')\, \mathrm{d}\mathbf{r}'. \tag{30}$$

4.1. Solution for the scalar Greens function

In order to utilize the Greens function as derived above, we must find an expression for the function p. The homogenous differential equation of (29) may be solved via the introduction of a cylindrical coordinate system for $\mathbf{r}$, (r, θ), centred at the origin and the use of separation of variables [5]. The eigenfunction expansion of p is given by (see the appendix for the full derivation)

$$p(r, \theta, \mathbf{r}') = \frac{A_0}{\sqrt{2\pi}} J_0(kr) + \sum_{n=1}^{\infty} \left(A_n J_n(kr) \frac{\cos(n\theta)}{\sqrt{\pi}} + B_n J_n(kr) \frac{\sin(n\theta)}{\sqrt{\pi}} \right), \tag{31}$$

where J_n is the nth order Bessel function of the first kind, and the coefficients A_n and B_n are given by

$$\begin{aligned} A_n(\mathbf{r}, \mathbf{r}') &= \frac{-1}{\sqrt{\pi} J_n(ka)} \int_{-\pi}^{\pi} g_{fs}(a, \theta, \mathbf{r}') \cos(n\theta)\, \mathrm{d}\theta \\ B_n(\mathbf{r}, \mathbf{r}') &= \frac{-1}{\sqrt{\pi} J_n(ka)} \int_{-\pi}^{\pi} g_{fs}(a, \theta, \mathbf{r}') \sin(n\theta)\, \mathrm{d}\theta, \end{aligned} \tag{32}$$

where a is the radius of the cylinder. In our case,

$$g_{fs}(\mathbf{r}, \mathbf{r}') = \frac{1}{4j} H_0^{(2)}(k|\mathbf{r} - \mathbf{r}'|), \tag{33}$$

where $H_0^{(2)}$ is the zeroth-order Hankel function of the second kind, (note this is the 2D homogenous space Greens function corresponding to the use of e^{jwt} time dependency).

Closed-form expressions for A_n and B_n may be derived (see the appendix), and are given by

$$A_n = \frac{-\pi}{4j\sqrt{\pi} J_n(ka)} \left[J_n(k|\mathbf{r}'|)\, \mathrm{e}^{-jn\phi'} H_n^{(2)}(ka) + J_{-n}(k|\mathbf{r}'|)\, \mathrm{e}^{jn\phi'} H_{-n}^{(2)}(ka) \right] \tag{34}$$

and

$$B_n = \frac{-\pi}{4\sqrt{\pi} J_n(ka)} \left[J_n(k|\mathbf{r}'|)\, \mathrm{e}^{-jn\phi'} H_n^{(2)}(ka) + J_{-n}(k|\mathbf{r}'|)\, \mathrm{e}^{jn\phi'} H_{-n}^{(2)}(ka) \right], \tag{35}$$

where $H_n^{(2)}$ is the nth order Hankel function of the second kind, and ϕ' is the angle associated with the position vector $\mathbf{r}'$. These closed-form expressions significantly reduce computation time for the Greens function.

Figure 2 shows a plot of the magnitude of the Greens function for a frequency of 1 GHz inside a PEC cylinder of radius 20 cm with a lossless background of $\epsilon_r = 3$. For comparison purposes, the regular free-space Greens function is plotted in the same figure. Note that both Greens functions are singular at the source, but the discretization used in figure 2 avoids these singularities. However, it is instructive to note how much more energy is located throughout the PEC cylinder than for unbounded space.

In the context of computational electromagnetics, it is important to eliminate the surface integral in (25). The elimination of this integral allows for the application of standard (frequency domain) electromagnetic computational techniques, i.e. only a minimal change

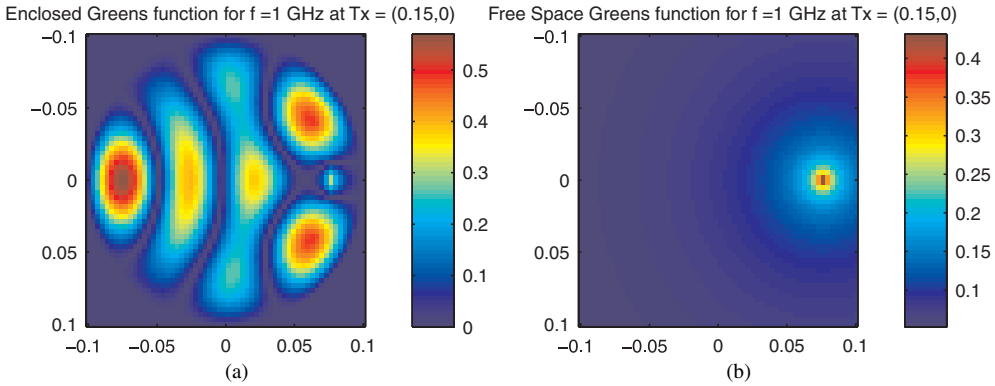

Figure 2. Example of Greens functions. (a) Greens function for a source at (0.15, 0) with a PEC cylinder of radius 20 cm and frequency of 1 GHz. (b) Unbounded Greens function at the same location and frequency. Significantly more energy is located inside the PEC cylinder.

is required to switch an extant computational code to the new physical situation. In addition, we note that the only singularity of the Greens function, g, is located in the free-space term. This is due to the fact that the term satisfies a homogenous differential equation. This means that standard methods of extracting singularities [3, 4] in method of moments (MoM) codes remain unchanged. This advantage is not a feature of other forms of the Greens function (see, for e.g. [2, section 14.6.2]). To evaluate integrals of the function p, we may utilize standard quadrature techniques, due to the fact that p is a smooth function.

5. Implementation of the modified Greens function in the MR-CSI

The use of the modified Greens function in MR-CSI requires little or no changes at the conceptual level. All that is required is the use of the modified Greens function in the functional to be minimized (14). However, the switch in Greens functions does affect the numerical implementation. From a computational perspective, the most important aspects of the PEC Greens function are that (1) the Greens function cannot be written in the form $g(\mathbf{r}, \mathbf{r}') = g(\mathbf{r} - \mathbf{r}')$ and (2) the fields do not decay monotonically as the distance between $\mathbf{r}$ and $\mathbf{r}'$ increases. As these two properties are the core requirements required for the FFT and fast multipole acceleration methods respectively, the usual techniques used to make $O(N^2)$ (in memory and computational time) matrix operations into fast $O(N \log N)$ matrix operations are not applicable to matrices which result from the use of this Greens function. The lack of these two desirable properties is not formulation dependent, in that they represent the actual physics of EM point sources in a PEC enclosed structure (the existence of standing waves). Thus, a simple re-formulation of the Green function will not allow these acceleration methods to be applied.

Despite these apparent difficulties with the enclosed problem, a solution which does scale as in computation time is reported in [14], thus the problem is tractable. However, for simplicity, the results in this paper are generated with all matrix multiplication in the format.

In practice, the infinite sum in equation (31) must be truncated. This is accomplished by taking enough terms in the series until it converges to within some error tolerance.

6. Computational results

Several different synthetic data sets based on a 2D model have been generated to test the efficacy of the enclosed microwave tomographic method. The incident field for every transmitter was a line source which was parallel to the axis of the scatterer, i.e. the incident field was taken to be the Greens function. The data were generated with a 2D method of moments (MoM) solver using pulse basis functions and point matching [23].

In order to test the inversion algorithm's performance in the presence of noise, 10% RMS additive white noise was added to all scattered field measurements as follows [22]:

$$f_k^{\text{Noisy}} = f_k^{\text{meas}} + \max\left(\left|f_k^{\text{meas}}\right|, \forall f_k^{\text{meas}}\right)\frac{Ns}{\sqrt{2}}(\alpha + j\beta), \tag{36}$$

where α and β are uniformly distributed random numbers between -1 and 1, and Ns is the desired fraction of noise (in this paper, $Ns = 0.1$). For every inversion example, the conditions $\text{Re}(\chi) > 0$ and $-\text{Im}(\chi) < 0$ were enforced at every step of the MR-CSI algorithm.

For image clarity, all results in figures 3–6 display the negative of the imaginary part of the contrast, $-\text{Im}(\chi) = \epsilon''/\epsilon_b$. Furthermore, for all reconstructions displayed in figures 3–6, we calculated the L_1, L_2 and L_∞ vector norms based on the exact permittivity, χ_{exact}. The vector norms are normalized by the norm of the exact contrast, and are discretized versions of the norms for the continuous case

$$L_p = \frac{\|\chi_{\text{exact}}(\mathbf{r}) - \chi_{\text{recon}}(\mathbf{r})\|_p}{\|\chi_{\text{exact}}(\mathbf{r})\|_p}, \tag{37}$$

where $\chi_{\text{recon}}(\mathbf{r})$ is the reconstructed contrast. These vector norms are given in table 1. Due to the fact that forward and inverse grids are not identical, the discretized versions of (37) were calculated by interpolating onto a finer and finer mesh until the norm converged.

6.1. Square scatterer

For the first numerical example, we consider a simple scenario consisting of a square lossy scatterer. The operating frequency was 1 GHz, and the scatterer is embedded in a PEC cylinder of radius 20 cm. The lossless background has a permittivity of $\epsilon_b = 3\epsilon_0$, where ϵ_0 is the permittivity of free space. This low value of relative permittivity was chosen to avoid excessively small wavelengths which overburden the $O(N^2)$ computations. The scatterer is illuminated by ten transmitters located evenly on a circle of radius 15 cm. The scattered field is measured at 40 receiver points placed on a circle of radius 16 cm. The inversion region D is a square with edges of 20 cm length located in the centre of the PEC cylinder. The scatterer consists of a square object with sides of length 10 cm and a contrast of $\chi = 2.0 - j1.0$. Thus, the object has edges slightly larger than 0.5 λ. The exact contrast is shown in part (a) of figure 3. The forward data were generated on a grid of 30×30 placed over D. In order to avoid an inverse crime the inversion grid was selected to be 29×29 cells: this ensures that numerical quadrature points for the inverse and forward problem are distinct. The inversion results after 1024 iterations of the MR-CSI algorithm with the enclosed (PEC bounded) Greens function are shown in part (b) of figure 3.

The reconstruction results show a good, but not perfect reconstruction of the object. The overall shape of the scatterer is clearly visible, and the magnitude of both the real and imaginary parts of the contrast are close to the exact values. However, the edges of the object are slightly blurred, which is not unexpected given difference between the forward and inversion grids, and the real part of the reconstruction overshoots the exact value of 2.0.

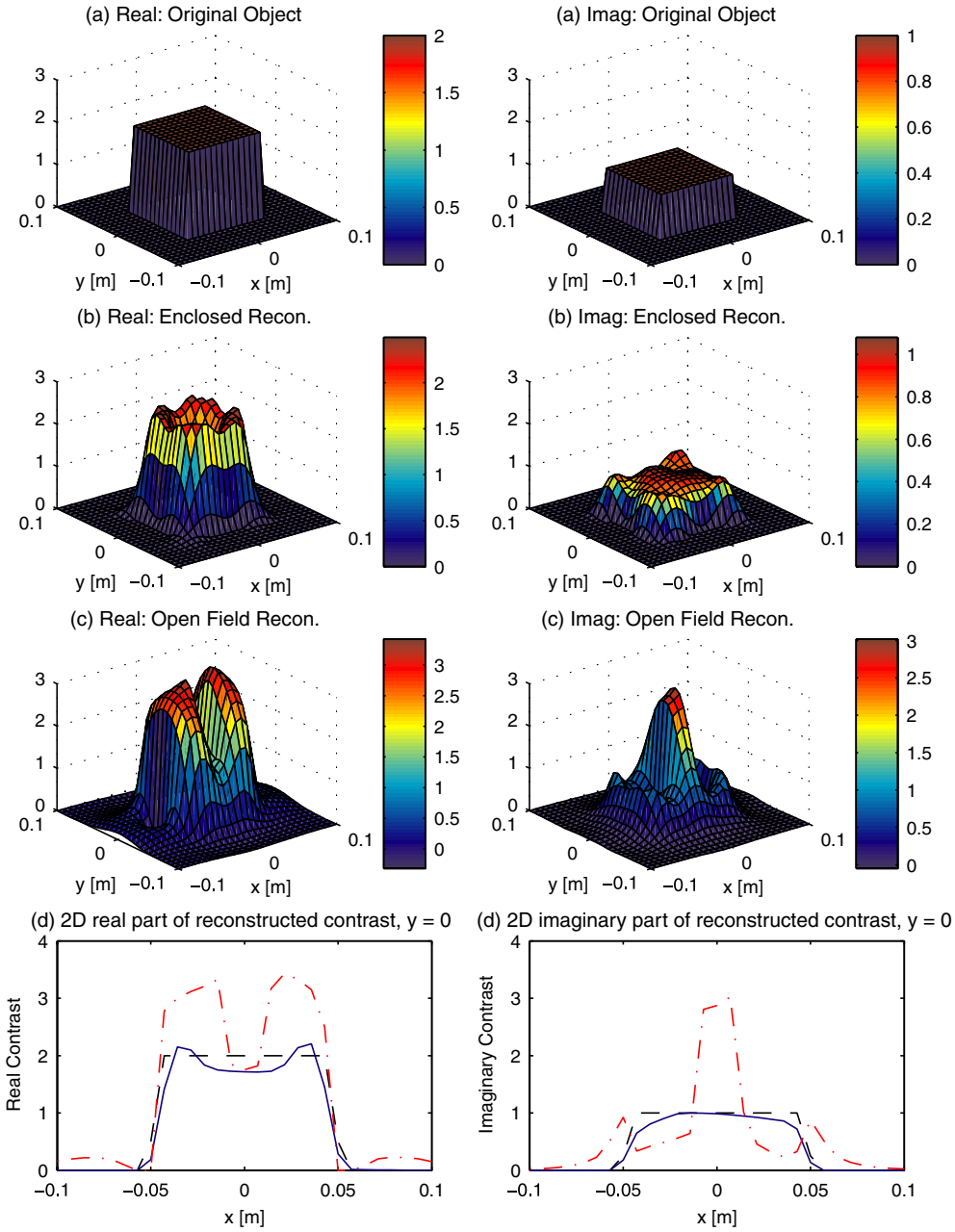

Figure 3. Square scatterer reconstruction after 1024 steps of the MR-CSI algorithm. (a) The exact contrast of the scatterer. (b) The MR-CSI reconstruction when the both forward data generation and inversion include a cylindrical PEC shield. (c) Reconstruction when both the forward data generation and inversion assume a free-space background. (d) A 2D cross section at $y = 0$ for (black dash line) exact, (blue solid line) enclosed reconstruction, (red dash dot) free-space reconstruction.

For comparison purposes, new data were generated for the equivalent unbounded problem: all input parameters for the forward solver were kept the same, except the PEC cylinder was

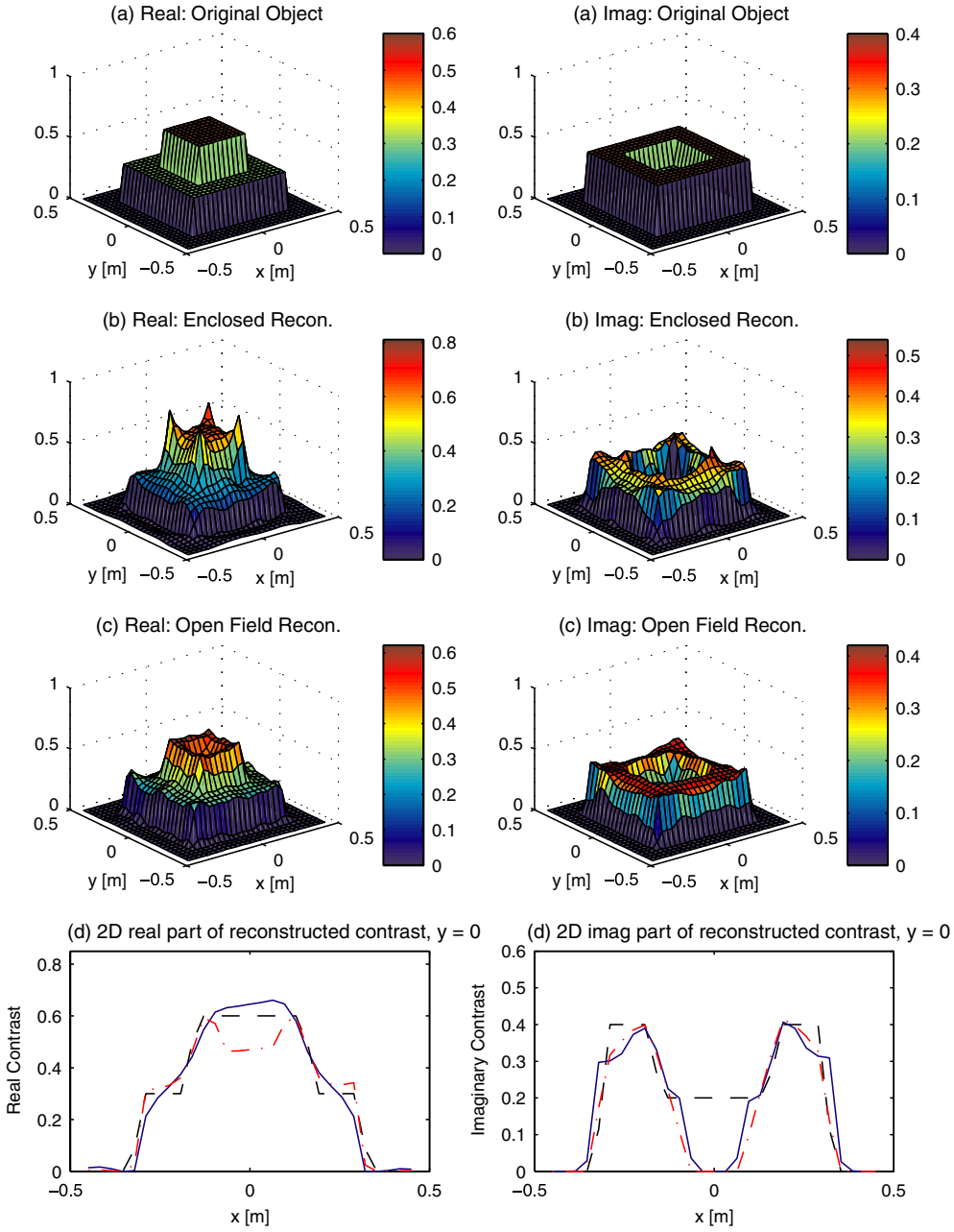

Figure 4. Low-contrast concentric squares after 1024 steps of the MR-CSI algorithm. (a) The exact contrast of the scatterer. (b) The MR-CSI reconstruction when the both forward data generation and inversion include a cylindrical PEC shield. (c) Reconstruction when both the forward data generation and inversion assume a free-space background. (d) A 2D cross section at $y = 0$ for (black dash line) exact, (blue solid line) enclosed recon., (red dash dot) free-space recon.

removed (i.e. the regular unbounded-space Greens function was used). Thus, the target was embedded in an infinite medium filled with the background permittivity of $\epsilon_b = 3\epsilon_0$. The

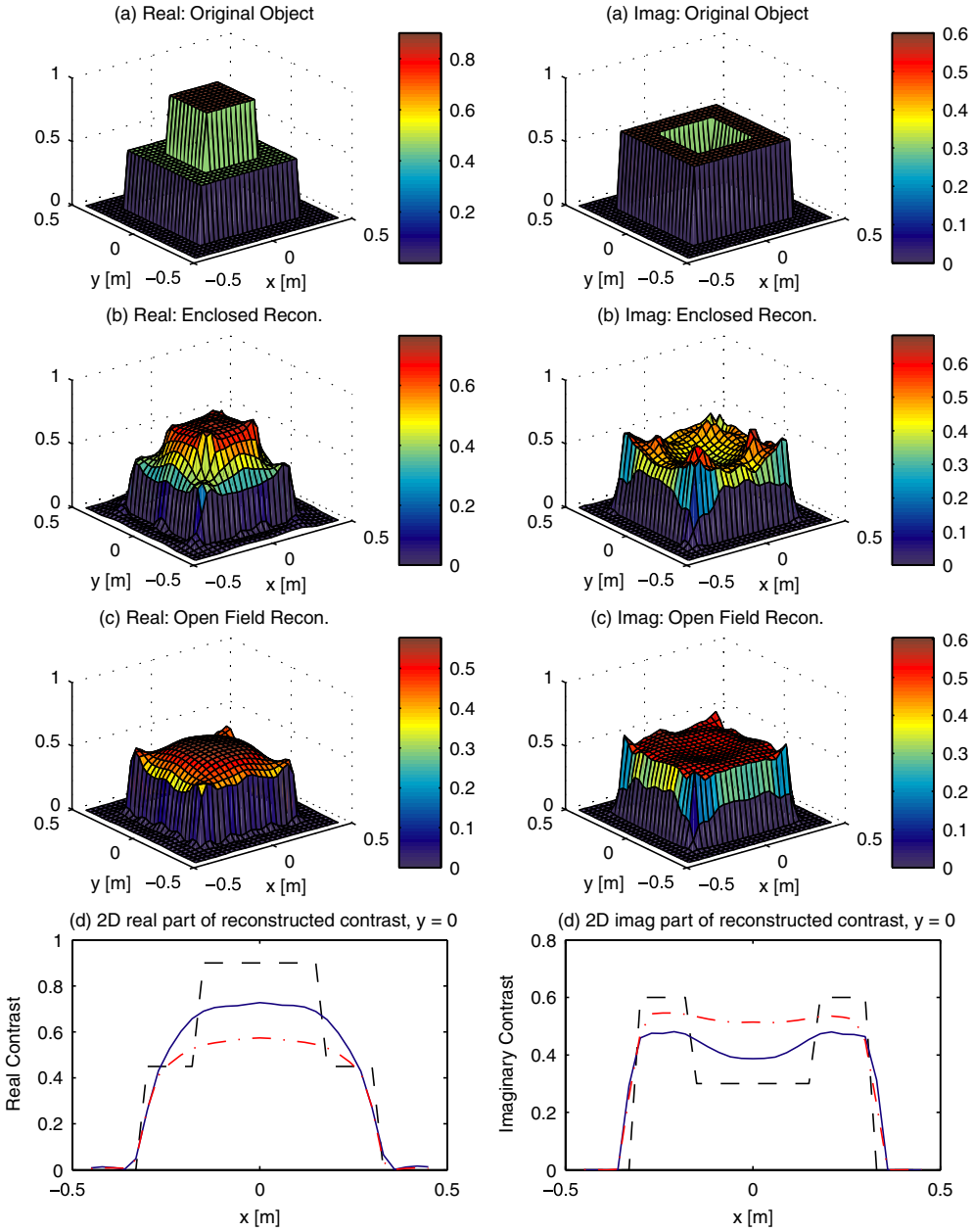

Figure 5. Mid-contrast concentric squares after 1024 steps of the MR-CSI algorithm. (a) The exact contrast of the scatterer. (b) The MR-CSI reconstruction when the both forward data generation and inversion include a cylindrical PEC shield. (c) Reconstruction when both the forward data generation and inversion assume a free-space background. (d) A 2D cross section at $y = 0$ for (black dash line) exact, (blue solid line) enclosed recon., (red dash dot) free-space recon.

forward data were then inverted in the MR-CSI reconstruction using the regular unbounded-space Greens function. The reconstruction from the unbounded-space forward and inverse solvers is shown in part (c) of figure 3. Although the reconstruction shows the approximate

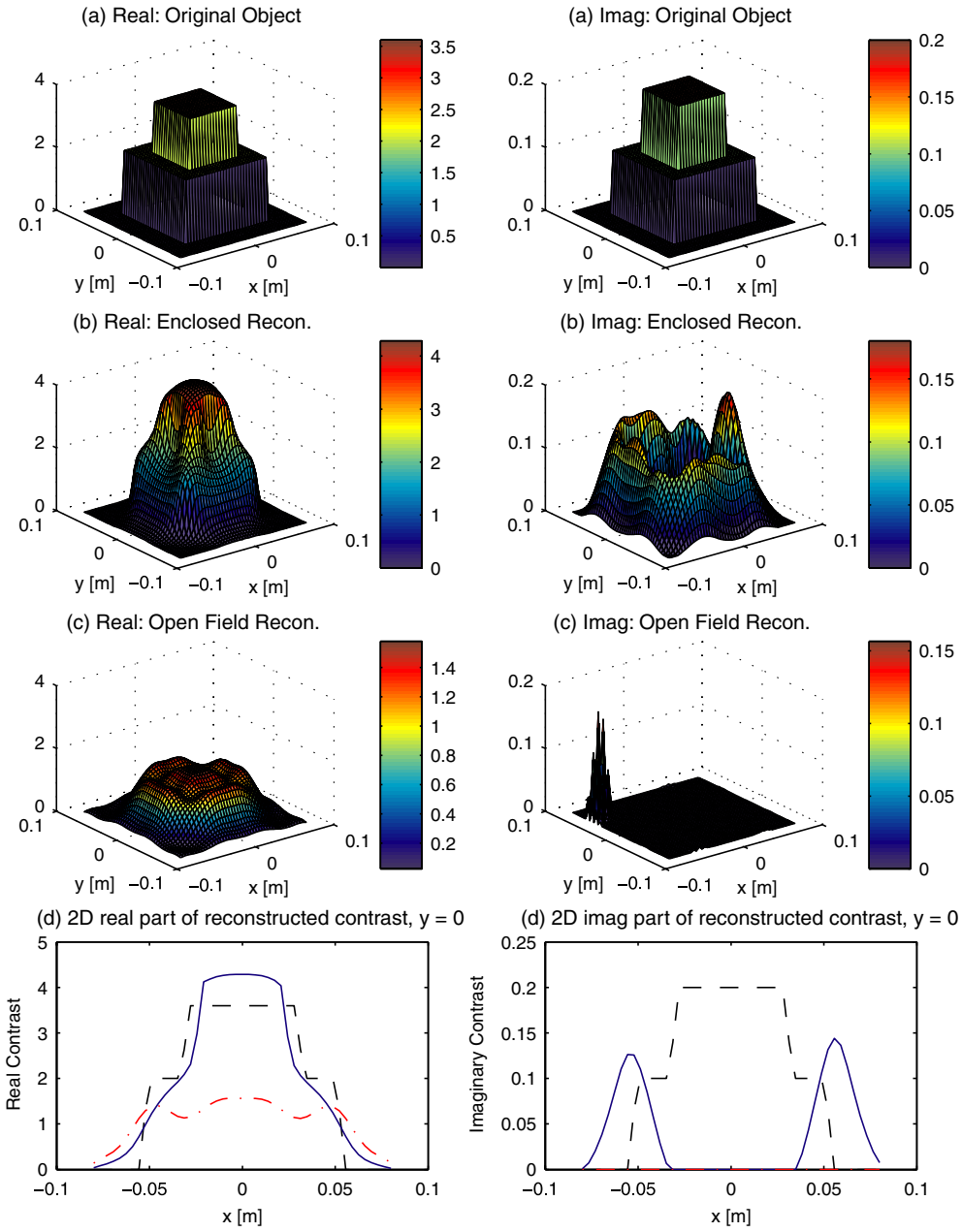

Figure 6. Mutli-frequency concentric squares after 1024 steps of the MR-CSI algorithm. (a) The exact contrast of the scatterer. (b) The MR-CSI reconstruction when the both forward data generation and inversion include a cylindrical PEC shield. (c) Reconstruction when both the forward data generation and inversion assume a free-space background. (d) A 2D cross section at $y = 0$ for (black dash line) exact, (blue solid line) enclosed recon., (red dash dot) free-space recon.

outline of the scatterer, it significantly overshoots the correct values for both the real and imaginary parts of the contrast. More importantly, the reconstruction shows significant structure inside the scatterer where no such structure exists (e.g. $-\mathrm{Im}(\chi)$ varies from 0 to 3

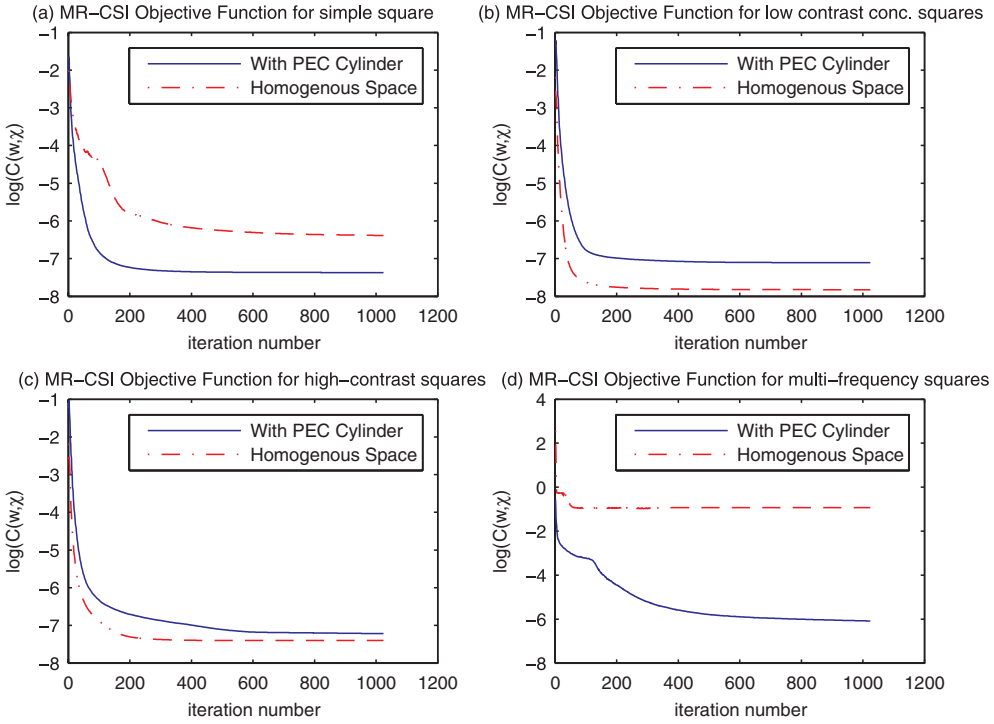

Figure 7. The MR-CSI objective function, $C(w, \chi)$ versus iteration number for (a) simple square, (b) low-contrast concentric squares, (c) high-contrast concentric squares and (d) multi-frequency concentric squares reconstruction.

inside the scatterer). If one was searching for an inhomogeneity in a target (e.g. a tumour in a breast), this would render the reconstruction untrustworthy.

For further clarity, two-dimensional cross sections of the two reconstructions are shown in part (d) of figure 3. The value of the MR-CSI objective function, $C(w, \chi)$, for these two reconstructions is shown in part (a) of figure 7. The objective function is lower when the PEC cylinder is present. In addition, as shown in table 1 the L_1, L_2 and L_∞ vector norms are significantly improved when the PEC cylinder is present.

In this case, it is clear that the use of the bounded-region tomographic system has significantly improved the reconstruction. We hypothesize that the reconstruction is improved because more energy is located inside the lossy scatterer due to the bounding of the energy by the enclosure. However, it is unclear exactly how this extra energy effects the inversion algorithm. This is an area of ongoing research for which we make speculative remarks in the conclusion.

6.2. Concentric squares

6.2.1. Low contrast concentric squares. Next, we consider the same scattering object as has been used as a test case for the MR-CSI method [6, 7]. The scatterer consists of two concentric squares, with an inner square having sides of length λ, with a contrast of $\chi = 0.6 - j0.2$, embedded in an exterior square having sides of 2λ and contrast $\chi = 0.3 - j0.4$. The exact contrast profile is shown in part (a) of figure 4. The imaging region D consists of a square

Table 1. Relative vector norms of reconstructed contrast functions.

	Reconstruction with PEC enclosure	Reconstruction without PEC enclosure
Simple squares (figure 3)		
L_1 error	25.2%	60.6%
L_2 error	24.6%	47.2%
L_3 error	73.3%	90.7%
Low-contrast concentric squares (figure 4)		
L_1 error	23.1%	15.5%
L_2 error	22.5%	17.3%
L_3 error	45.9%	40.0%
High-contrast concentric squares (figure 5)		
L_1 error	26.2%	26.0%
L_2 error	24.4%	29.4%
L_3 error	36.8%	47.9%
Multi-frequency concentric squares (figure 6)		
L_1 error	27.9%	68.6%
L_2 error	24.8%	59.3%
L_3 error	51.6%	69.9%

having sides of length 3λ. A single frequency of 1 GHz was utilized, and free space was assumed for the background. The forward data were generated on a grid of 31×31. Thirty transmitters were spaced evenly on a circle of radius $2.33\lambda = 70$ cm, and 40 receivers were placed evenly on a circle of radius $2.17\lambda = 65$ cm. The scatterer was surrounded by a PEC cylinder of radius 90 cm or approximately 3λ.

The data were inverted via the MR-CSI algorithm with the bounded Greens function. As before, the inversion mesh was selected to have 29×29 elements. The reconstruction after 1024 iterations of the MR-CSI algorithm is shown in part (b) of figure 4. The reconstruction is not as good as for the single square case, but the inner square is clearly visible.

Again, the forward data were re-generated for the case where no PEC cylinder was present, but keeping every other parameter of the forward solver the same. These unbounded free-space data were inverted via the MR-CSI algorithm with the unbounded Greens function, and the results are shown in part (c) of figure 4. Two-dimensional cross section results are shown in part (d) of figure 4. The MR-CSI objective function versus the iteration number is shown in part (b) of figure 7. The three vector norms of the reconstructions are also given in table 1.

In this case, the reconstruction results are slightly better for the unbounded case, as shown by the vector norms, and the final value of the MR-CSI objective function. However, both reconstructions provide reasonable results in that the overall structure of the scatterer is visible and the value of the vector norms are low in both cases. We speculate that this is due to the fact that the contrast is lower than the previous case of the single square. These results do not exactly match previously published reconstructions with the MR-CSI method, but this discrepancy is due to different transmitter and receiver configurations and noise levels (more noise was added than in [7]).

6.2.2. Mid contrast concentric squares. The concentric square example was run again, but this time with a higher contrast scatterer, with a contrast of 150% of the previous example for

both inner and outer squares. The dimensions were kept identical. The inner square now has a contrast of $\chi = 0.9 - j0.3$, and the outer square has a contrast of $\chi = 0.45 - j0.6$. Both the bounded Greens function and unbounded forward solvers were run again, and the data were inverted via the appropriate MR-CSI program. All computational parameters were unchanged from the previous concentric squares case.

The reconstruction results are shown in figure 5, the MR-CSI objective functions in part (c) of figure 7, and the vector-norm errors in table 1. The results are very close for all metrics, but slightly better for the enclosed case. While neither reconstruction resolves the two squares perfectly, the inner square is unresolved when the unbounded-space Greens function is utilized. Although the exact contrast of the inner square is not obtained in the bounded reconstruction, the outline is at least visible.

6.3. High-contrast multi-frequency concentric squares

A high-contrast scatterer was created which consists of two concentric squares with the inner square having sides of length 6 cm, and the outer square having sides of length 10 cm. The contrast for the inner cylinder is given by $\chi = 3.6 - j0.2$ at a frequency of 0.5 GHz, and the outer square has a contrast of $\chi = 2.0 - j0.1$ (also at 0.5 GHz). The scatterer was embedded in a background medium with permittivity of $\epsilon_b = 3\epsilon_0$. The object was illuminated by 12 sources, placed on a square centred at the origin with sides of 15 cm, at frequencies of 0.5, 1 and 2 GHz. Thus, at the lowest frequency, the scatterer had dimensions of $L \approx 0.29\lambda$, and at the highest frequency, $L \approx 1.15\lambda$. Forty receivers were utilized on a circle of radius 16 cm. For the forward solver, the scatterer was discretized into 45×45 cells, and for the inverse solver, a grid of 47×47 was utilized. For the first experiment, the scatterer was surrounded by a PEC surface of radius 20 cm. For the second, the scatterer was embedded in an infinite homogenous background medium.

The contrast reconstructions are shown in figure 6, the MR-CSI objective function is shown in part (b) of figure 7, and the vector-norm errors for the reconstructions are given in table 1. The results show that the enclosed system performs much better than the unbounded one for every single metric. While neither reconstruction is perfect, the reconstruction with the PEC cylinder clearly shows the general shape of the object for the real part of the contrast, and the values of the squares are quite close. Both reconstructions fail for the imaginary part the contrast.

6.4. Matching medium artefacts produced by unbounded domain MWT

It is interesting to note that many researchers who utilize the unbounded domain microwave tomography also use a matching media, which, for practical reasons, is of finite extent. In theory, this invalidates the use of the unbounded homogenous domain Greens function. Good results have been obtained due to fact that the loss associated with the matching media allows very little energy to reach the boundaries of the matching region. However, due to the finite dynamic range of practical MWT systems, it is desirable to not introduce a lossy matching medium. In this section, we attempt to quantify the artefacts introduced when the unbounded domain Greens function is utilized in a lossless matching media MWT system.

The simulated problem for this case is shown in figure 8. We simulate a tomographic imaging system which has a cylindrical matching fluid of $\epsilon_b = 4\epsilon_0$ with radius 30 cm. Inside the holding tank are two cylindrical scatterers of radius 4 cm centred at $(x, y) = (\pm 5, 0)$ cm and with permittivity of $\epsilon = 5\epsilon_0$. Thirty transmitters are located on a circle of radius 25 cm,

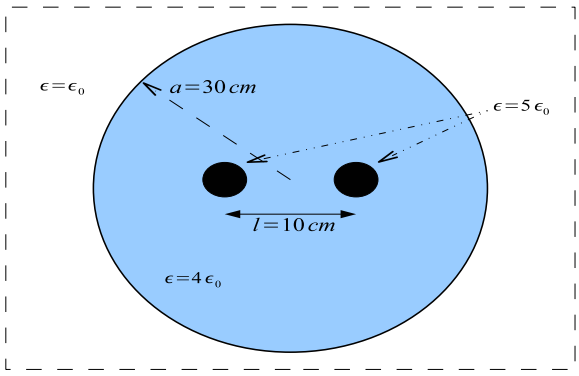

Figure 8. Simulation of a tomographic imaging system without a PEC boundary. Two cylinders of radius 4 cm are embedded in the tank of matching fluid with $\epsilon = 4\epsilon_0$. The matching medium is surrounded by unbounded free space.

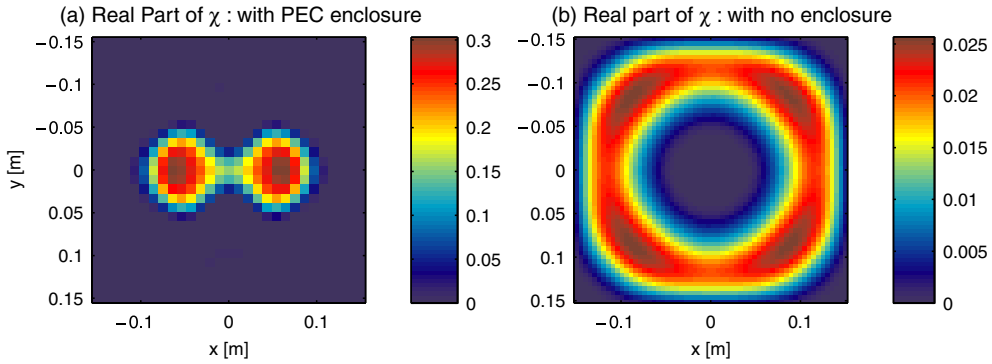

Figure 9. Reconstruction of two cylinders with and without PEC. (a) Reconstruction when a PEC cylinder surrounds the matching medium and is taken into account in the inversion. (b) Reconstruction when the matching medium is surrounded by free space, and an infinite matching medium is assumed in the inversion. The reconstruction in (b) is completely wrong.

and 40 receivers are located on a circle of radius 23 cm. An operation frequency of 1 GHz was utilized for this example.

Two computational experiments were performed. In the first, the embedding medium was located within a PEC cylinder. Data were generated, and inverted via the MR-CSI algorithm. The inversion results for the real part of the contrast are shown in part (a) of figure 9. The imaginary reconstruction is not included as the contrast is very close to zero (as required). As can be seen, the two cylinders are reconstructed reasonably well.

In the second computational experiment, synthetic data were generated taking into account the finite matching medium. That is, we assumed that some fictitious EM transparent tank was holding in the matching medium. The data were generated, and inverted via the MR-CSI algorithm assuming that the inhomogeneities were embedded in an infinite background medium. Thus, the reflections from the edge of the embedding medium are not taken into account in the inversion, and will produce artefacts in the reconstruction. The reconstruction results are shown in part (b) of figure 8. As can be seen, this reconstruction is completely

wrong due to the fact that the reflections from the edge of the matching medium completely overwhelm the scattering from the two cylinders in the tank. Therefore, an additional advantage of the enclosed MWT system is that these artefacts are not produced. These inversion results would improve with the use of a lossy matching medium, but, as stated previously, this would come at the cost of adding undesirable loss to the scattering experiment.

7. Conclusion

We have considered a method of microwave tomographic imaging where the imaging region is surrounded by an electrically conductive surface. For the case where this surface is a PEC cylinder, we have derived a version of the enclosed-domain Greens function which is amenable for use in existing computational solvers with only small modifications. This Greens function was implemented in both a MoM forward solver for producing synthetic data and in the MR-CSI algorithm. The use of this Greens function precludes the use of standard "fast" $O(N \log N)$ computational techniques, and currently all computations are implemented using algorithms with $O(N^2)$ computational complexity, although this problem is tractable [14].

Several different synthetically generated examples were shown in which the use of a PEC cylinder to surround the scattering object improved the inversion results over the usual method of embedding the scatterer in an infinite background medium. The improvements were not seen in every case, but, the PEC enclosure did not significantly degrade the results in any case. We hypothesize that the improvements which are present are due to the fact that more energy is located inside the scatterer due to the reflections from the PEC surface, but these remarks are only speculative as the exact connection between this energy and successful inversion is poorly understood. Another hypothesis is that the standing wave or resonant nature of the field distribution inside the enclosure contributes to the improved imaging. Another hypothesis is that the norm of the Greens function operator effects these improvements. It has already been shown in [24] that the sufficient conditions for the convergence of both the distorted Born iterative method and Born iterative inversion methods are related to the norm of the Greens function operator. In a second paper, we will analyze this improvement in more detail.

We also showed the artefacts which are generated with the use of a tomographic imaging system which has a finite matching medium and a reconstruction algorithm which does not take the finite nature of the matching fluid into account. The use of the external PEC cylinder in the tomographic system, combined with the use of the related Greens function in the inversion algorithm does not produce such artefacts.

Acknowledgments

The authors would like to acknowledge the support of the National Sciences and Engineering Research Council (NSERC) of Canada, Manitoba Health Research Council, and CancerCare Manitoba.

Appendix A. Separation of variables derivation for the PEC bounded Greens function

We are concerned with solving the 2D differential equation

$$\begin{aligned} &\nabla^2 p(\mathbf{r}, \mathbf{r}') + k^2 p(\mathbf{r}, \mathbf{r}') = 0 \qquad \mathbf{r} \in V \\ &p(\mathbf{r}, \mathbf{r}') = -g_{fs}(\mathbf{r}, \mathbf{r}') \qquad \mathbf{r} \in S \end{aligned}, \tag{A.1}$$

where S is a circle of radius a. We first introduce the cylindrical coordinates $\mathbf{r} = (r, \theta)$, and write the Helmholtz equation in these cylindrical coordinates,

$$\begin{aligned} &\frac{\partial^2 p}{\partial r^2} + \frac{1}{r}\frac{\partial p}{\partial r} + \frac{1}{r^2}\frac{\partial^2 p}{\partial \theta^2} + k^2 p = 0 \qquad 0 < r < a, \quad -\pi < \theta < \pi \\ &p(a, \theta, \mathbf{r}') = -g_{fs}(a, \theta, \mathbf{r}') \end{aligned} . \tag{A.2}$$

Assuming that p may be written as

$$p(r, \theta) = R(r)H(\theta), \tag{A.3}$$

we note that

$$\frac{R''}{R} + \frac{1}{r}\frac{R'}{R} + \frac{1}{r^2}\frac{H''}{H} + k^2 = 0, \tag{A.4}$$

where prime and double prime denote first and second derivatives, respectively. Due to the fact that R and H are independent, we note

$$r^2\frac{R''}{R} + r\frac{R'}{R} + r^2k^2 = -\frac{H''}{H} = \alpha = \text{constant}, \tag{A.5}$$

which results in two separated ordinary differential equations (ODE), solvable through the application of the boundary and periodicity conditions. The first ODE is given by

$$H'' + \alpha H = 0, \tag{A.6}$$

and the periodicity requirement gives the conditions

$$H(-\pi) = H(\pi) \qquad H'(-\pi) = H'(\pi). \tag{A.7}$$

Equations (A.6) and (A.7) constitute a Sturm–Louiville system [5] with eigenvalues

$$\alpha = n^2, \tag{A.8}$$

where n is a non-negative integer, with corresponding orthonormal eigenfunctions

$$\begin{aligned} &\frac{1}{\sqrt{2\pi}} \qquad n = 0 \\ &\frac{1}{\sqrt{\pi}}\cos(n\theta) + \frac{1}{\sqrt{\pi}}\sin(n\theta) \qquad n > 0. \end{aligned} \tag{A.9}$$

The remaining differential equation is

$$r^2R'' + rR' + (r^2k^2 - n^2)R = 0. \tag{A.10}$$

Equation (A.10) is Bessels equation of order n. We know that the solution to this equation must be a summation of the Bessel functions of the form

$$J_n(kr),\ Y_n(kr),\ H_n^{(1)}(kr),\ H_n^{(2)}(kr), \tag{A.11}$$

where $J_n(kr)$ is the nth order Bessel function of the first kind, $Y_n(kr)$ is the nth order Bessel function of the second kind, and $H_n^{(1)}(kr)$ and $H_n^{(2)}(kr)$ are the nth order Hankel functions of the first and second kind, respectively. However, since the solution p is non-singular inside the PEC region, solutions to R must be of the form

$$R_n(r) = J_n(kr), \tag{A.12}$$

as $J_n(kr)$ is the only solution of Bessels equation which is non-singular.

Thus, general solutions of the form $p(a, \theta; \mathbf{r}') = R(r)H(\theta)$ may be now written as

$$p(a, \theta, \mathbf{r}') = \frac{A_0}{\sqrt{2\pi}}J_0(kr) + \sum_{n=1}^{\infty}\left(A_nJ_n(kr)\frac{\cos(n\theta)}{\sqrt{\pi}} + B_nJ_n(kr)\frac{\sin(n\theta)}{\sqrt{\pi}}\right), \tag{A.13}$$

where the coefficients, A_0, A_n and B_n are chosen to satisfy the boundary conditions, namely

$$p(a, \theta, \mathbf{r}') = -g_{fs}(a, \theta, \mathbf{r}'), \tag{A.14}$$

or

$$p(a, \theta, \mathbf{r}') = \frac{A_0}{\sqrt{2\pi}} J_0(ka) + \sum_{n=1}^{\infty} \left(A_n J_n(ka) \frac{\cos(n\theta)}{\sqrt{\pi}} + B_n J_n(ka) \frac{\sin(n\theta)}{\sqrt{\pi}} \right). \tag{A.15}$$

Making use of the orthonormal nature of the eigenfunctions of $H(\theta)$, we multiply both sides of (A.15) by $1/\sqrt{2\pi}$, and integrate from $\theta = -\pi$ to $\theta = \pi$, and arrive at

$$A_0 = \frac{-1}{\sqrt{2\pi}\, J_n(ka)} \int_{-\pi}^{\pi} g_{fs}(a, \theta, \mathbf{r}')\, \mathrm{d}\theta. \tag{A.16}$$

To determine A_n, we multiply both sides of (A.15) by $\cos(m\theta)/\sqrt{\pi}$ and integrate over θ, which results in

$$A_n = \frac{-1}{\sqrt{\pi}\, J_n(ka)} \int_{-\pi}^{\pi} g_{fs}(a, \theta, \mathbf{r}') \cos(n\theta)\, \mathrm{d}\theta. \tag{A.17}$$

And by similar argument

$$B_n = \frac{-1}{\sqrt{\pi}\, J_0(ka)} \int_{-\pi}^{\pi} g_{fs}(a, \theta, \mathbf{r}') \sin(n\theta)\, \mathrm{d}\theta. \tag{A.18}$$

These two integrals may be derived in a closed form by considering the identity ([2, section 11.4.2])

$$H_0^{(2)}(k|\mathbf{r} - \mathbf{r}'|) = \left\{ \begin{array}{ll} \displaystyle\sum_{m=-\infty}^{m=\infty} J_m(kr) H_m^{(2)}(kr')\, \mathrm{e}^{jm(\theta-\theta')} & r \leqslant r' \\ \displaystyle\sum_{m=-\infty}^{m=\infty} J_m(kr') H_m^{(2)}(kr)\, \mathrm{e}^{jm(\theta-\theta')} & r \geqslant r' \end{array} \right\}, \tag{A.19}$$

where r, r' and θ, θ' are the cylindrical coordinates for $\mathbf{r}$ and $\mathbf{r}'$, respectively. For the integrals in (A.17) and (A.18), $r > r'$, and we may write

$$A_n = \frac{-1}{4j\sqrt{\pi}\, J_n(ka)} \int_{-\pi}^{\pi} \left(\sum_{m=-\infty}^{m=\infty} J_m(kr') H_m^{(2)}(kr)\, \mathrm{e}^{jm(\theta-\theta')} \right) \cos(n\theta)\, \mathrm{d}\theta, \tag{A.20}$$

which equals

$$A_n = \frac{-1}{4j\sqrt{\pi}\, J_n(ka)} \left(\sum_{m=-\infty}^{m=\infty} J_m(kr') H_m^{(2)}(kr)\, \mathrm{e}^{-jm\theta'} \right) \int_{-\pi}^{\pi} \mathrm{e}^{jm\theta} \cos(n\theta)\, \mathrm{d}\theta, \tag{A.21}$$

and since

$$\int_{-\pi}^{\pi} \mathrm{e}^{jm\theta} \cos(n\theta)\, \mathrm{d}\theta = \pi \qquad \text{if} \quad |n| = m \tag{A.22}$$

and is 0 otherwise, A_n is equal to the expression given in (34). The derivation for B_n proceeds in an analogous manner.

References

[1] Collin R E 1990 *Field Theory of Guided Waves* 2nd edn (Piscataway, NJ: IEEE)

[2] Balanis C 1989 *Advanced Engineering Electromagnetics* (New York: Wiley)

[3] Wilton D, Rao S, Glisson A, Schaubert D, Al-Bundak O and Butler C 1984 Potential integrals for uniform and linear source distributions on polygonal and polyhedral domains *IEEE Trans. Antennas Propag.* **32** 276–81

[4] Richmond J H 1965 Scattering by a dielectric cylinder of arbitrary cross section and shape *IEEE Trans. Antennas Propag.* **13** 334–41
[5] Trim D 1990 *Applied Partial Differential Equations* (Boston, MA: PWS-Kent Publishing Company)
[6] van den Berg P M and Kleinman R 1997 Contrast source inversion method *Inverse Problems* **13** 1607–20
[7] van den Berg P M, van Broekhoven A L and Abubakar A 1999 Extended contrast source inversion *Inverse Problems* **15** 1325–44
[8] Abubakar A, van den Berg P M and Mallorqui J J 2002 Imaging of biomedical data using a multiplicative regularized contrast source inversion method *IEEE Trans. Microw. Theory Tech.* **50** 1761–71
[9] Semenov S Y, Bulyshev A E, Abubakar A, Posukh V G, Sizov Y E, Souvorov A E, van den Berg P M and Williams T C 2005 Microwave-tomographic imaging of the high-dielectric-contrast objects using different image-reconstruction approaches *IEEE Trans. Microw. Theory Tech.* **53** 2284–94
[10] Abubakar A, van den Berg P M and Habashy T M 2005 Application of the multiplicative regularized contrast source inversion method on TM- and TE-polarized experimental Fresnel data *Inverse Problems* **21** S5–13
[11] Bloemenkamp R F, Abubakar A and van den Berg P M 2001 Inversion of experimental multi-frequency data using the contrast source inversion method *Inverse Problems* **17** 1611–22
[12] Geffrin J M and Joisel A 2002 Comparison of measured and simulated incident and scattered fields in a 434 Mh scanner *Proc. of the 22th URSI General Assembly 2002 (Maastricht, The Netherlands, 17–24 August)*
[13] van den Berg P M and Fokkema J T 2003 Removal of undesired wavefields related to the casing of a microwave scanner *IEEE Trans. Microw. Theory Tech.* **51** 187–92
[14] Franchois A and Tijhuis A G 2003 A quasi-Newton reconstruction algorithm for a complex microwave imaging scanner environment *Radio Sci.* **38** 12.1–12.13
[15] Williams T C, Fear E C and Westwick D T Tissue sensing adaptive Radar for breast cancer detection-investigations of an improved skin-sensing method *IEEE Trans. Microw. Theory Tech.* **54** 1308–14
[16] Semenov S Y *et al* 1999 Three dimensional microwave tomography: experimental prototype of the system and vector Born reconstruction method *IEEE Trans. Biomed. Eng.* **46** 937–46
[17] Devaney A J 1982 A filtered backpropagation algorithm for diffraction tomography *Ultrason. Imaging* **4** 336–50
[18] Broquetas A, Romeu J, Rius J M, Elias-Fuste A R, Cardama A and Jofre L 1991 Cylindrical geometry: a further step in active microwave tomography *IEEE Trans. Microw. Theory Tech.* **39** 836–44
[19] Meaney P M, Fanning M W, Dun L, Poplack S P and Paulsen K D 2000 A clinical prototype for active microwave imaging of the breast *IEEE Trans. Microw. Theory Tech.* **48** 1841–53
[20] Chew W C and Wang Y M 1990 Reconstruction of two-dimensional permittivity distribution using the distorted Born iterative method *IEEE Trans. Med. Imaging* **9** 218–25
[21] Bulyshev A E, Souvorov A E, Semenov S Y, Svenson R H, Nazarov A G, Sizov Y E and Tatsis G P 2000 Three-dimensional microwave tomography. Theory and computer experiments in scalar approximation *Inverse Problems* **16** 863–75
[22] Abubakar A, van den Berg P M and Semenov S Y 2004 A robust iterative method for born inversion *IEEE Trans. Geosci. Remote Sens.* **42** 342–54
[23] Harrington R 1968 *Field Computation by Moment Methods* (Malabar, FL: Krieger)
[24] Jun S C and Jin Choi U Convergence Analyses of the born iterative and the distorted born iterative method *Numer. Funct. Anal. Optim.* **20** 301–16